

Metal-organic Frameworks Hexagonal Nanoplates: Bottom-up Synthesis, Topotactic Transformation and Efficient Oxygen Evolution Reaction

Yifan Lin,¹ Hao Wan,¹ Dan Wu,¹ Gen Chen,¹ Ning Zhang,¹ Xiaohe Liu,^{1*} Junhui Li,¹
Yijun Cao,^{2*} Guanzhou Qiu³ and Renzhi Ma^{4*}

¹ State Key Laboratory of Powder Metallurgy, School of Materials Science and Engineering, Central South University, Changsha, Hunan 410083, P. R. China.

² Henan Province Industrial Technology Research Institute of Resources and Materials, Zhengzhou University, Zhengzhou, Henan 450001, P. R. China.

³ School of Minerals Processing and Bioengineering, Central South University, Changsha, Hunan 410083, P. R. China.

⁴ International Center for Materials Nanoarchitectonics, National Institute for Materials Science, 1-1 Namiki, Tsukuba, Ibaraki 305-0044, Japan.

* Email: liuxh@csu.edu.cn

yijuncao@126.com

MA.Renzhi@nims.go.jp

Experimental Section

Materials. Nickel(II) nitrate ($\text{Ni}(\text{NO}_3)_2 \cdot 6\text{H}_2\text{O}$, >99 wt%), ferrous chloride ($\text{FeCl}_2 \cdot 4\text{H}_2\text{O}$, >99 wt%), 1,4-Diazabicyclo[2.2.2]octane (DABCO, >98 wt%), 1,4-dicarboxybenzene (HBDC, >98 wt%), N,N-dimethylformide (DMF, >98 wt%), acetonitrile (MeCN, >98 wt%), pyridine (>99.5 wt%) and 1 mol/L potassium hydroxide solution (1M KOH) were purchased from Wako Pure Chemical Industries, Ltd. All chemicals were used without further purification.

Characterizations. The crystal structures were characterized by X-ray diffraction with Cu $K\alpha$ radiation ($\lambda = 1.5405 \text{ \AA}$, Rigaku Ultima IV). The morphology was recorded with a JEOL JSM-6700F scanning electron microscopy (SEM). The high-resolution transmission electron microscope (HRTEM) images, selected area electron diffraction (SAED) and energy-dispersive spectroscopy (EDS) mapping were performed on a JEOL JEM-3100F TEM. The thickness of HXP was measured with a Seiko SPA 400 atomic force microscope (AFM). Thermogravimetric (TG) data was collected with a Rigaku TGA-8120 instrument at a heating rate of 10 °C/min in nitrogen gas. N_2 sorption isotherms were measured at 77 K adsorbates in a Quantachrome autosorb-1 analyzer. XPS data were recorded at a Physical Electronics XPS-5700 spectrometer with Al $K\alpha$ X-ray line (1486.6 eV).

Synthesis of Ni-based hexagonal nanoplates (HXP). The HXP could be fabricated via a facile oil bath method. $\text{Ni}(\text{NO}_3)_2 \cdot 6\text{H}_2\text{O}$ (0.2 mmol), HBDC (0.2 mmol) and DABCO (0.1 mmol) were dissolved in 40 mL DMF under ultrasonic for 15 min. Then 0.3 mL pyridine was added drop wise into the former solution. The solution was kept stirring for another 10 min before heated at 80 °C for 12 hrs. After cooling down to the room temperature, solid product in green was collected by centrifugation. The solid was then washed with DMF and MeCN for several times and dried at 50 °C under vacuum. Nanorods (HXR) was synthesized with 0.1 mL pyridine. Nanodisks (HXD) with thickness around 100 nm was obtained with 0.2 mL pyridine. Blank control product was fabricated in absence of pyridine.

Conversion into N-doped Ni@carbon nanoplates. For the preparation of N-doped

Ni@carbon nanoplatelets, the HXP was used as precursor for annealing with the protection of inert gas. The as-synthesized green precursor was placed in a tube furnace filled with nitrogen gas flow. The annealing temperature was set in the range of 500-900 °C at a rate of 2 °C per minute and kept for 2 h to yield a black product. The fabrication of catalysts deriving from HXD and HXR were carried out under annealing temperature of 800 °C only at a rate of 2 °C per minute and kept for 2 h to yield black products.

Physical adsorption for Fe-doped HXP. The Fe-doping was conducted via a facile magnetic stirring method with the addition of $\text{FeCl}_2 \cdot 4\text{H}_2\text{O}$ as Fe source. In a 70 mL vial, 50 mg HXP was firstly dispersed in 50 mL DMF. Then 1.25 mL of DMF solution with $\text{FeCl}_2 \cdot 4\text{H}_2\text{O}$ concentration in 10 mg/mL was added into the former suspension. The vial was sealed with parafilm and kept stirring for 2 h. The solid product was collected by centrifugation and washed with DMF and MeCN for several times before dried at 50 °C under vacuum.

Conversion into N-doped Ni/Fe@carbon nanoplates (Fe-doped HXP@NC800). The Fe-doped HXP precursor was placed in a tube furnace filled with nitrogen gas flow. The annealing temperature was set to be 800 °C at a rate of 2 °C per minute and kept for 2 h to yield a black product.

Electrocatalytic Measurements. The catalyst powder (2 mg) was dispersed in a mixture of deionized water/ethanol solution (0.7 mL, 3:4 v/v) with 10 μL 10 wt% Nafion solution by sonicating for over 30 min. 5 μL of the ink was loaded on a glassy carbon (GC) electrode with a diameter of 3 mm (loading 0.2 mg cm^{-2}) and dried at 100 °C. Electrocatalytic measurements were carried out on CH Instruments model 760E electrochemical workstation using a three-electrode system. A coiled platinum wire was served as the counter electrode and a Hg/HgO electrode acted as reference electrode, respectively. The electrolyte was 1M KOH aqueous solution (pH = 13.5). The working electrode was kept rotating at a rate of 1600 rpm during the measurements. All polarization curves were obtained with 95% iR correction at the scan rate of 5 mV s^{-1} . Electrochemical impedance spectroscopy (EIS) data were recorded with the frequency range of 0.1~100000 Hz at the potential of 1.448 V vs

Hg/HgO. Tafel slope was calculated according to $\eta = a + b \times \log j$. Here, a is a constant and b refers to Tafel slope. The current density j was normalized to the geometrical area. The overpotential η was transformed from the measured potential $E_{\text{Hg}/\text{HgO}}$ using the following formula: $\eta = E_{\text{Hg}/\text{HgO}} + 0.059\text{pH} + 0.098 - 1.23$. For the measurement of $i-t$ curve, the sample was coated on a $1 \times 2 \text{ cm}^2$ graphite foil with a loading mass of 0.4 mg cm^{-2} as working electrode.

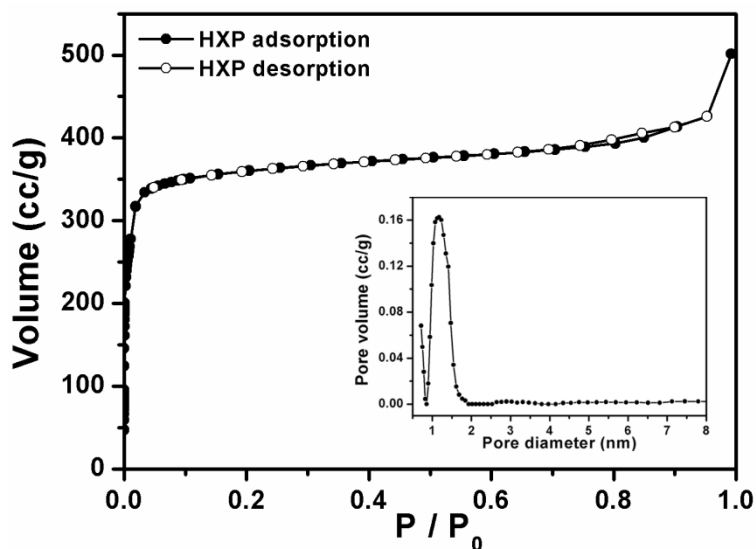


Figure S1 N₂ sorption isotherm of HXP at 77 K with inset pore size distribution.

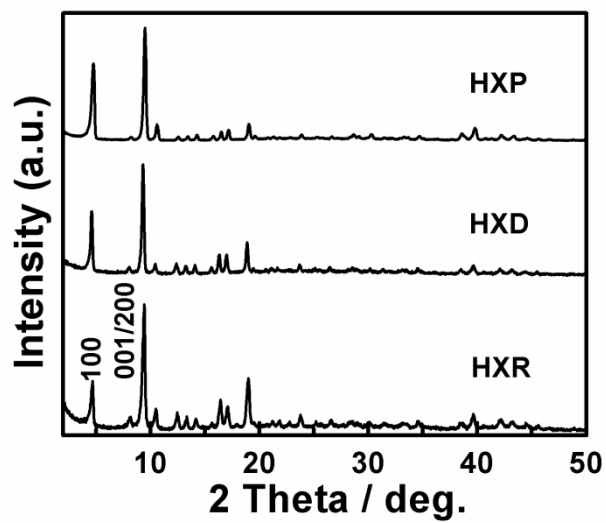


Figure S2 Comparison of XRD pattern for HXP, HXD and HXR.

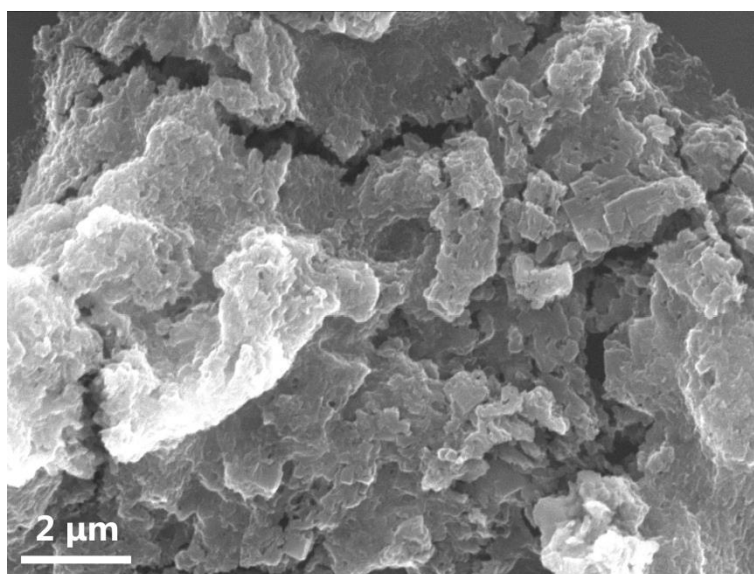


Figure S3 SEM image of blank control product without pyridine.

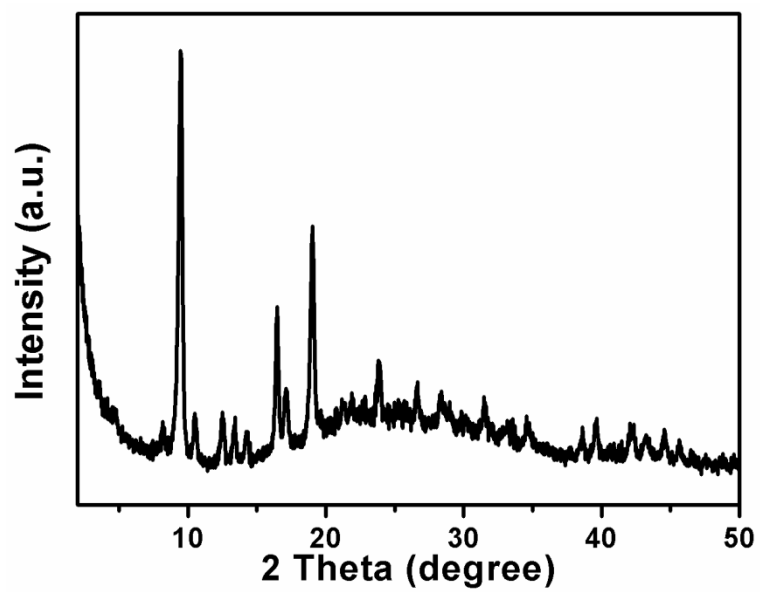


Figure S4 XRD pattern of blank control product without pyridine.

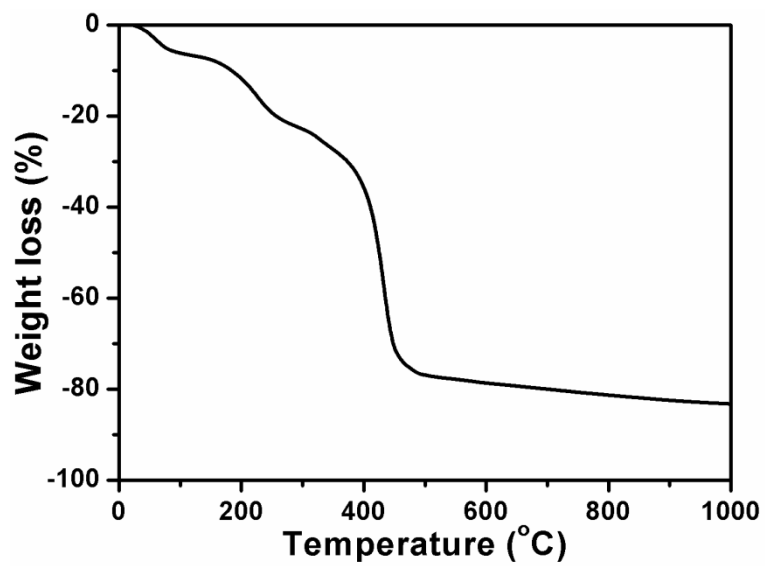


Figure S5 TG curve of HXP.

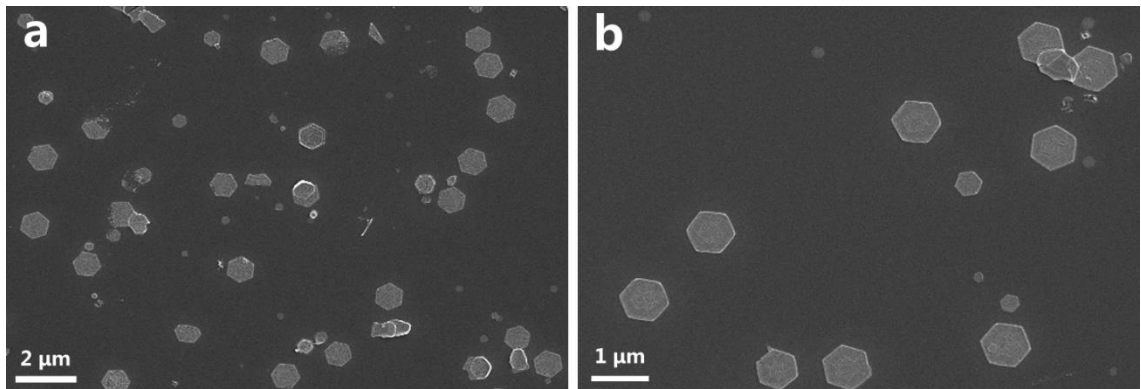


Figure S6 SEM images of HXP@NC800 with (a) low and (b) high magnification.

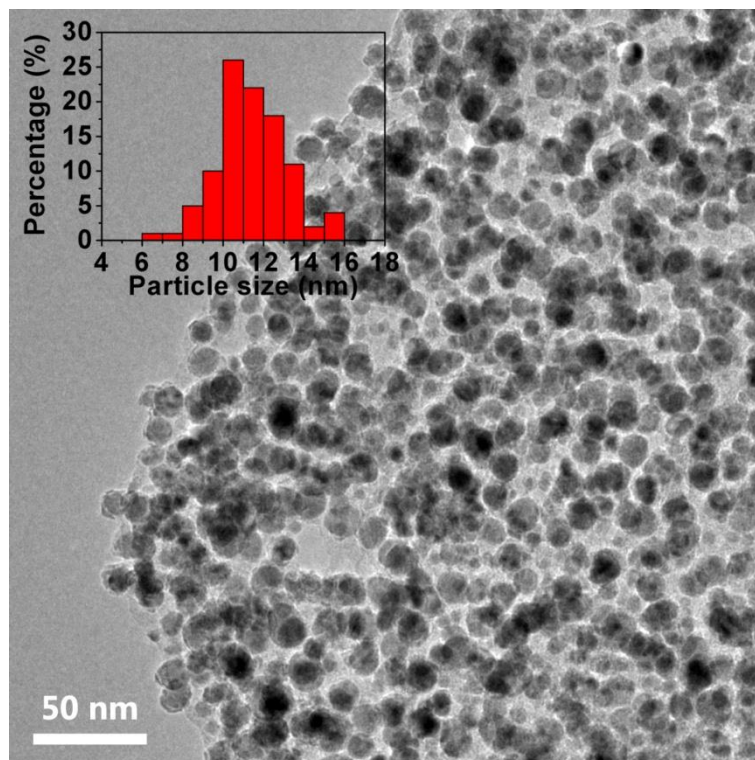


Figure S7 TEM image of HXP@NC800 with the distributions of particle sizes shown in the inset.

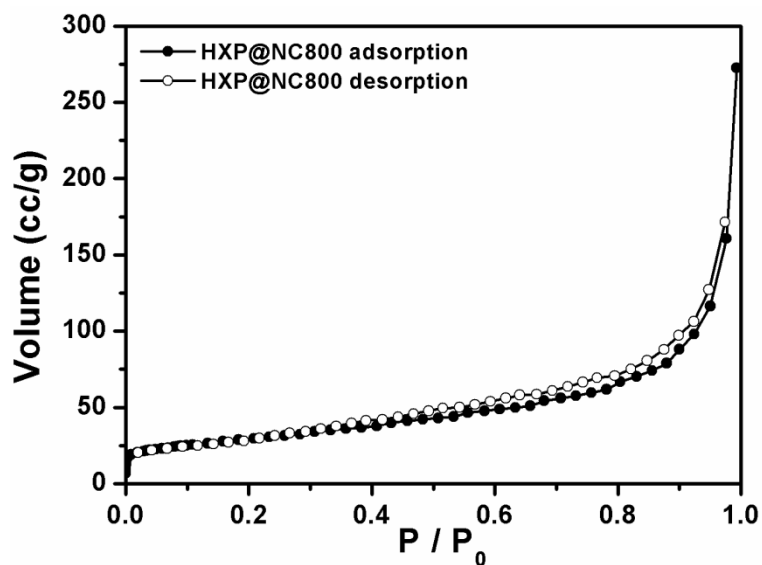


Figure S8 N_2 sorption isotherm of HXP@NC800 at 77 K.

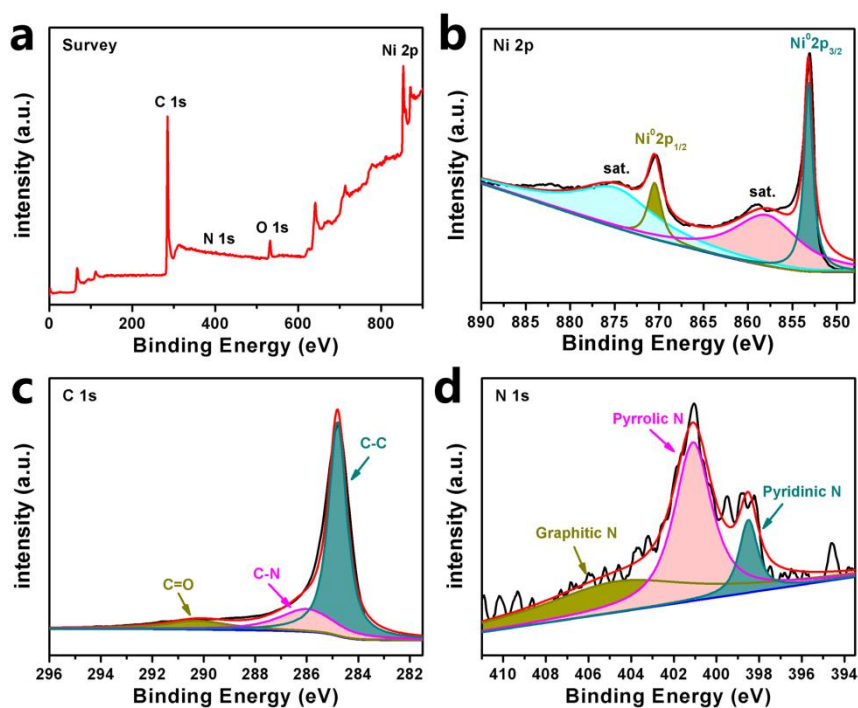


Figure S9 (a) XPS survey spectrum of HXP@NC800. High-resolution (b) Ni 2p, (c) C 1s, and (d) N 1s XPS spectra of HXP@NC800. The peak for oxygen was also detected because of the surface oxidation when the sample was exposed to air.

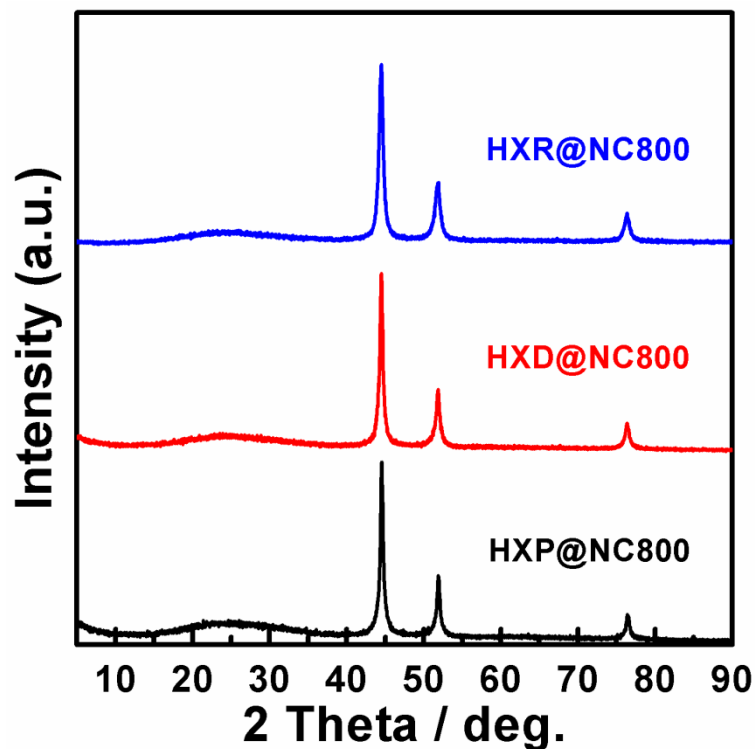


Figure S10 Comparison of XRD patterns for HXP@NC800, HXD@NC800 and HXR@NC800.

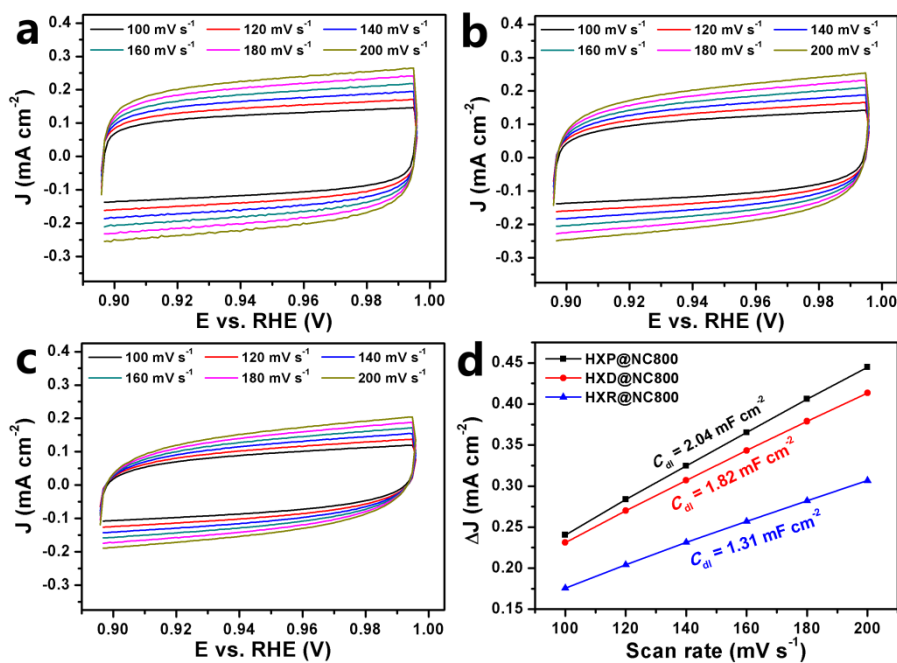


Figure S11 Cyclic voltammetry curves for (a) HXP@NC800, (b) HXD@NC800 and (c) HXR@NC800; (d) the current density difference as a function of scan rate in the region of 0.9~1.0 V vs. RHE.

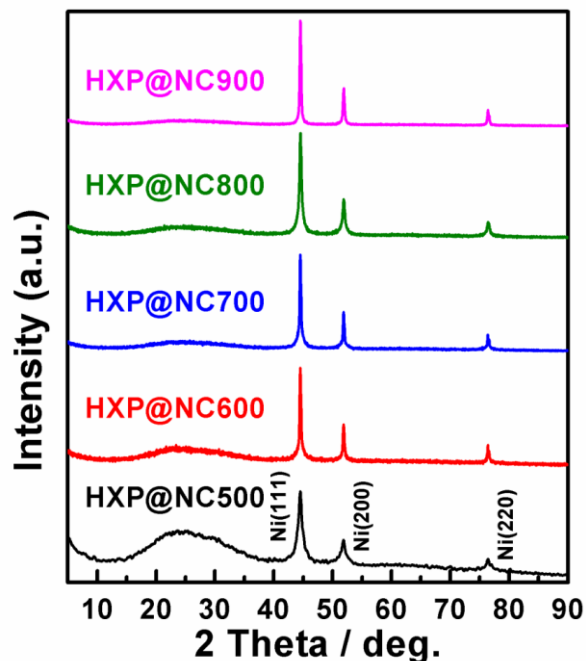


Figure S12 Comparison of XRD patterns for N-doped Ni@carbon composites annealed under 500, 600, 700, 800 and 900 °C (defined as HXP@NC500, HXP@NC600, HXP@NC700, HXP@NC800 and HXP@NC900).

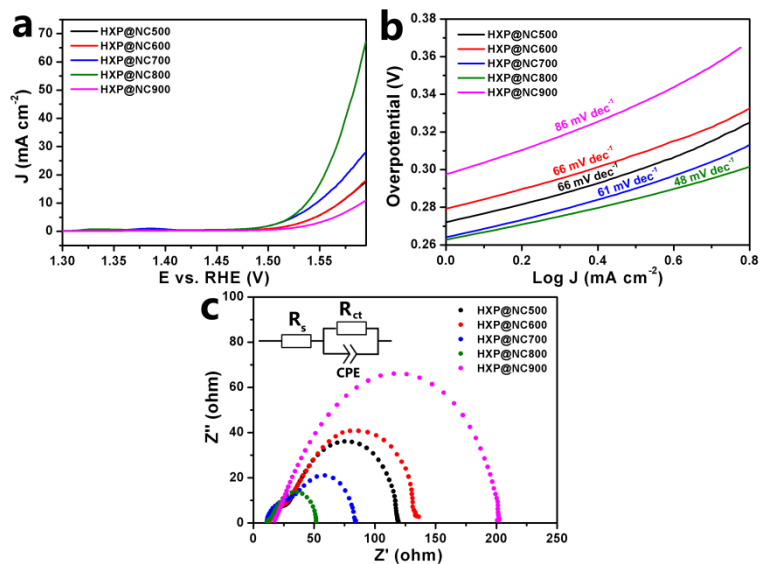


Figure S13 Comparison of OER activity for N-doped Ni@carbon composites. (a) LSV curves at a scan rate of 5 mV s⁻¹. (b) Tafel plots. (c) Nyquist plots and the fitting equivalent circuit model.

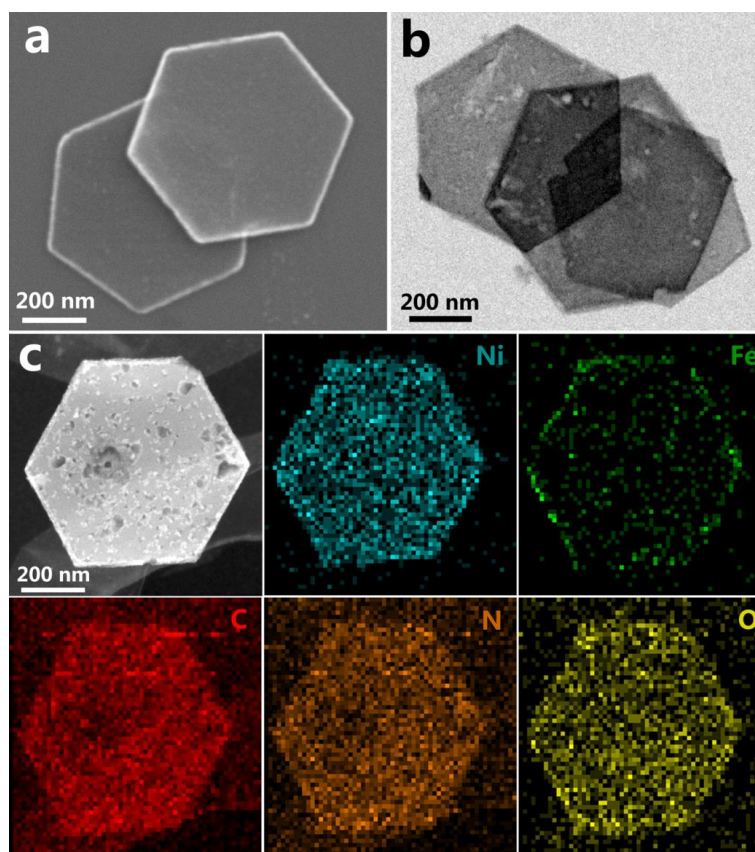


Figure S14 Morphology and element distribution of Fe-doped HXP. (a) SEM image, (b) TEM image and (c) EDS mapping of Fe-doped HXP. The hexagonal morphology was retained after Fe-doping. Meanwhile, the EDS mapping depicts the homogeneous distribution of Ni, Fe, C, N and O without cracks or aggregation, indicating uniform permeation of Fe^{2+} ions into the network, as well as the doping N atoms. The actual Fe/Ni atomic ratio was determined to be 0.19, which is smaller than the designed value of 0.58. The incomplete adsorption might be attributed to the competition between the solvent molecules and Fe ions, as well as probable charge repulsion from the metal sites.

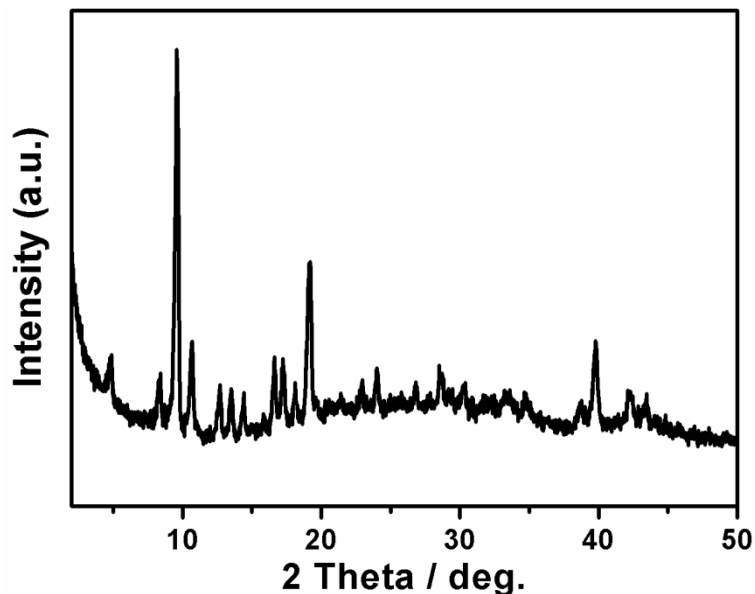


Figure S15 XRD pattern of Fe-doped HXP. All reflection peaks are identical with the undoped HXP, determining that no obvious collapse of crystal structure during Fe^{2+} doping process.

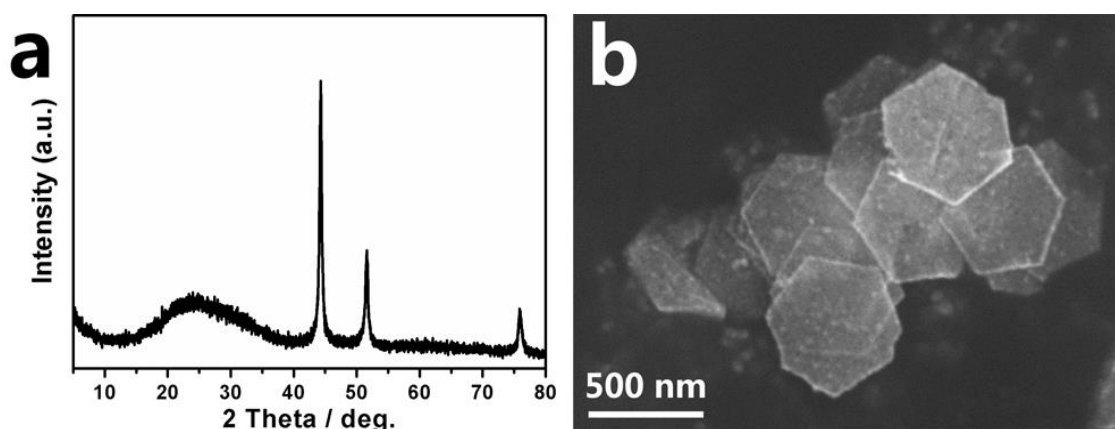


Figure S16 (a) XRD pattern and (b) SEM image of Fe-doped HXP@NC800. Same with HXP@NC800, the XRD pattern could be indexed to metallic Ni, referring to the formation of Ni/Fe alloy core in the composite. The SEM image shows entire hexagonal pieces with rough face and clear edges, indicating the successful synthesis of N-doped Ni/Fe@NC800 electrochemical catalyst.

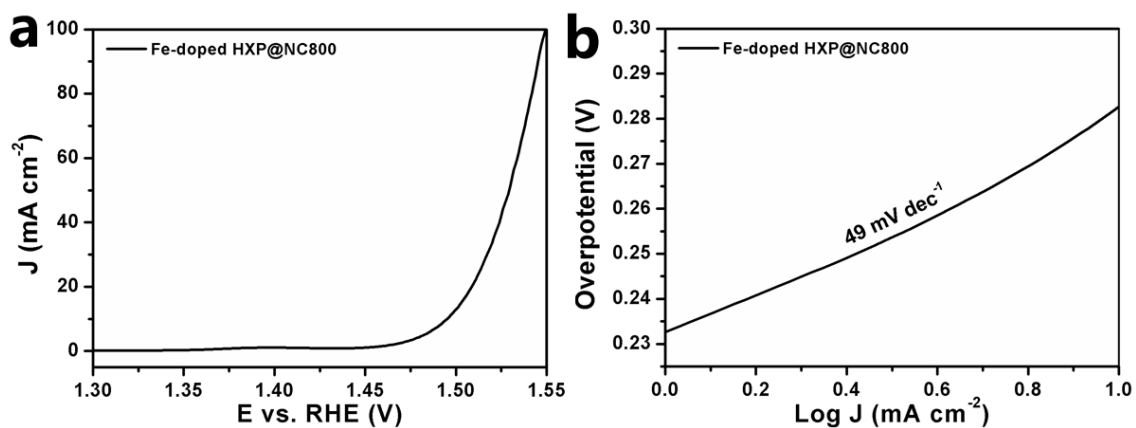


Figure S17 (a) LSV curve and (b) Tafel plots of Fe-doped HXP@NC800.

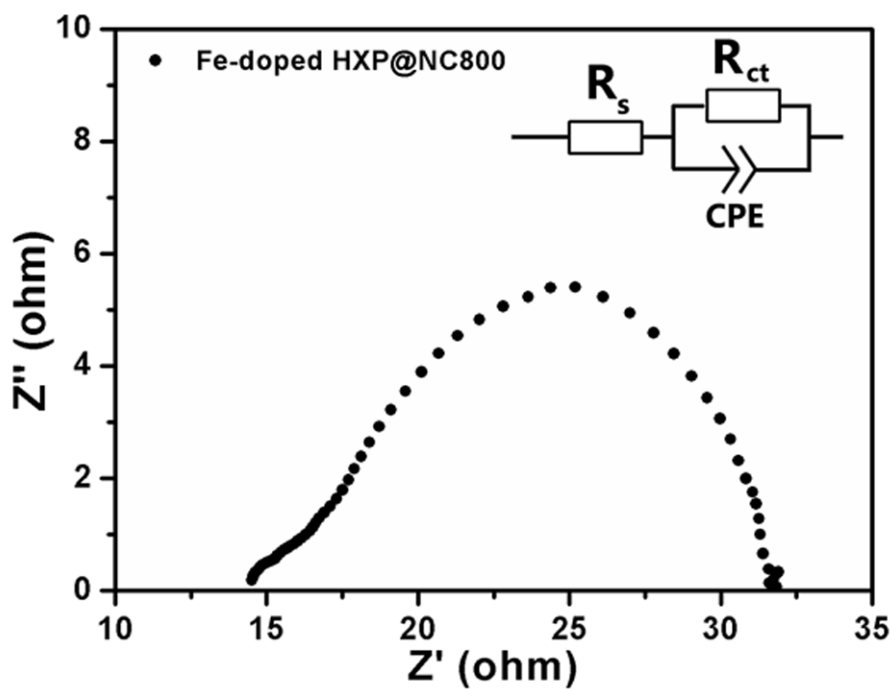


Figure S18 Nyquist plots and the fitting equivalent circuit model of Fe-doped HXP@NC800. The R_{ct} was calculated to be 17 Ω , which is much smaller than that of HXP@NC800.

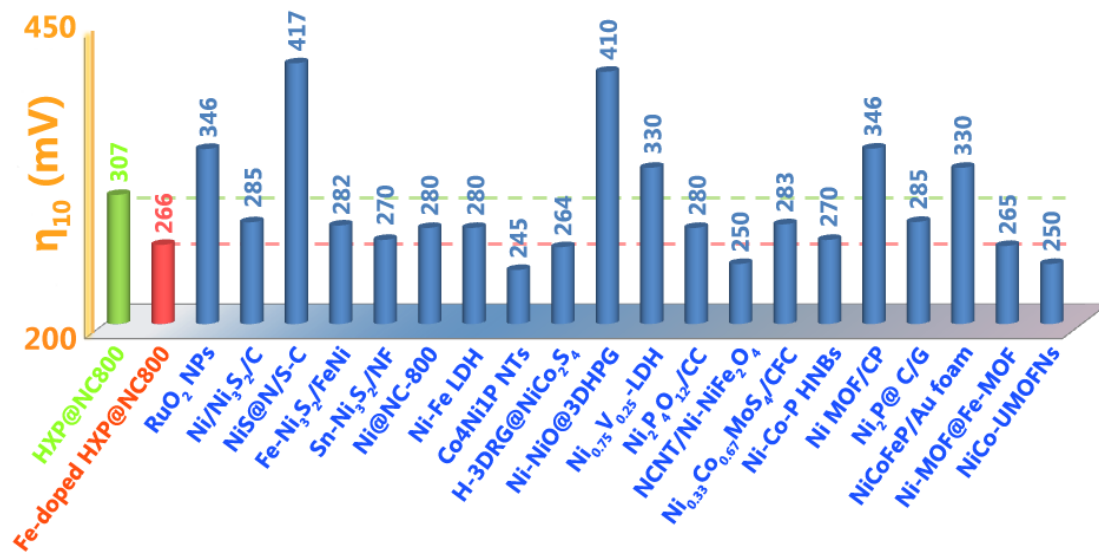


Figure S19 OER activity comparison between the HXP derived materials and recently advanced electrocatalysts in 1 M KOH electrolyte.

Table S1 OER comparison of Ni-based electrochemical catalysts in 1 M KOH.

Catalysts	Mass Loading (mg cm ⁻²)	Tafel slope (mV dec ⁻¹)	η_{10} (mV)	Reference
HXP@NC800	0.2	48	307	This work
Fe-doped HXP@NC800	0.2	49	266	This work
RuO ₂ nanoparticles	0.2	-	346	1
Ni/Ni ₃ S ₂ /carbon nanoplates	0.2	56	285	1
NiS@N/S-C	~0.57	48	417	2
Fe-Ni ₃ S ₂ /FeNi	-	54	282	3
Sn-Ni ₃ S ₂ /NF	-	56	270	4
Ni@NC-800	~0.31	45	280	5
Ni-Fe LDH hollow nanoprism	0.16	49	280	6
Co ₄ Ni ₁ P NTs	0.19	61	245	7
H-3DRG@NiCo ₂ S ₄	0.28	80	264	8
Ni-NiO@3DHPG	-	55	410	9
Ni _{0.75} V _{0.25} -LDH	0.14	50	330	10
Ni ₂ P ₄ O ₁₂ /CC	-	156	280	11
NCNT/NiFe ₂ O ₄ /Ni foam	-	51	250	12
Ni _{0.33} Co _{0.67} MoS ₄ /CFC	-	69	283	13
Ni-Co-P HNBS	2	76	270	14
Ni MOF/CP	0.48	64	346	15
Ni ₂ P@C/G	0.25	44	285	16
NiCoFeP/Au foam	-	60	330	17
Ni-MOF@Fe-MOF	0.2	82	265	18
NiCo-UMOFNs	0.2	42	250	19

Reference

- (1) Lin, Y.; Chen, G.; Wan, H.; Chen, F.; Liu, X.; Ma, R. 2D free-standing nitrogen-doped Ni-Ni₃S₂@carbon nanoplates derived from metal-organic frameworks for enhanced oxygen evolution reaction. *Small* **2019**, *15*, 1900348.
- (2) Yang, L.; Gao, M.; Dai, B.; Guo, X.; Liu, Z.; Peng, B. An efficient NiS@N/S-C hybrid oxygen evolution electrocatalyst derived from metal-organic framework. *Electrochim. Acta* **2016**, *191*, 813-820.
- (3) Yuan, C.; Sun, Z. T.; Jiang, Y. F.; Yang, Z. K.; Jiang, N.; Zhao, Z. W.; Qazi, U. Y.; Zhang, W. H.; Xu, A. W. One-step in situ growth of iron-nickel sulfide nanosheets on FeNi alloy foils: high-performance and self-supported electrodes for water oxidation. *Small* **2017**, *13*, 1604161.
- (4) Jian, J.; Yuan, L.; Qi, H.; Sun, X.; Zhang, L.; Li, H.; Yuan, H.; Feng, S. Sn-Ni₃S₂ ultrathin nanosheets as efficient bifunctional water-splitting catalysts with a large current density and low overpotential. *ACS Appl. Mater. Interfaces* **2018**, *10*, 40568-40576.
- (5) Xu, Y.; Tu, W.; Zhang, B.; Yin, S.; Huang, Y.; Kraft, M.; Xu, R. Nickel nanoparticles encapsulated in few-layer nitrogen-doped graphene derived from metal-organic frameworks as efficient bifunctional electrocatalysts for overall water splitting. *Adv. Mater.* **2017**, *29*, 1605957.
- (6) Yu, L.; Yang, J.; Guan, B.; Lu, Y.; Lou, X. Hierarchical hollow nanoprisms based on ultrathin Ni-Fe layered double hydroxide nanosheets with enhanced electrocatalytic activity towards oxygen evolution. *Angew. Chem.* **2018**, *57*, 172-176.
- (7) Yan, L.; Cao, L.; Dai, P.; Gu, X.; Liu, D.; Li, L.; Wang, Y.; Zhao, X. Metal-organic frameworks derived nanotube of nickel-cobalt bimetal phosphides as highly efficient electrocatalysts for overall water splitting. *Adv. Funct. Mater.* **2017**, *27*, 1703455.
- (8) Qin, K.; Wang, L.; Wen, S.; Diao, L.; Liu, P.; Li, J.; Ma, L.; Shi, C.; Zhong, C.; Hu, W.; Liu, E.; Zhao, N. Designed synthesis of NiCo-LDH and derived sulfide on heteroatom-doped edge-enriched 3D rivet graphene films for high-performance asymmetric supercapacitor and efficient OER. *J. Mater. Chem. A* **2018**, *6*, 8109-8119.
- (9) Ullah, N.; Zhao, W.; Lu, X.; Oluigbo, C. J.; Shah, S. A.; Zhang, M.; Xie, J.; Xu, Y. In situ growth of M-MO (M = Ni, Co) in 3D graphene as a competent bifunctional electrocatalyst for OER and HER. *Electrochim. Acta* **2019**, *298*, 163-171.
- (10) Fan, K.; Chen, H.; Ji, Y.; Huang, H.; Claesson, P. M.; Daniel, Q.; Philippe, B.; Rensmo, H.; Li, F.; Luo, Y.; Sun, L. Nickel-vanadium monolayer double hydroxide for efficient electrochemical water oxidation. *Nat. Commun.* **2016**, *7*, 11981.
- (11) Huang, J.; Sun, Y.; Zhang, Y.; Zou, G.; Yan, C.; Cong, S.; Lei, T.; Dai, X.; Guo, J.; Lu, R.; Li, Y.; Xiong, J. A new member of electrocatalysts based on nickel metaphosphate nanocrystals for efficient water oxidation. *Adv. Mater.* **2018**, *30*, 1705045.
- (12) Qin, Q.; Chen, L.; Wei, T.; Wang, Y.; Liu, X. Ni/NiM₂O₄ (M = Mn or Fe) supported on N-doped carbon nanotubes as trifunctional electrocatalysts for ORR, OER and HER. *Catalysis Science & Technology* **2019**, *9*, 1595-1601.
- (13) Hang, L.; Zhang, T.; Sun, Y.; Men, D.; Lyu, X.; Zhang, Q.; Cai, W.; Li, Y. Ni_{0.33}Co_{0.67}MoS₄ nanosheets as a bifunctional electrolytic water catalyst for overall water splitting. *J. Mater. Chem. A* **2018**, *6*, 19555-19562.
- (14) Hu, E.; Feng, Y.; Nai, J.; Zhao, D.; Hu, Y.; Lou, X. W. Construction of hierarchical Ni-Co-P hollow nanobricks with oriented nanosheets for efficient overall water splitting. *Energy Environ.*

Sci. **2018**, *11*, 872-880.

(15) Maruthapandian, V.; Kumaraguru, S.; Mohan, S.; Saraswathy, V.; Muralidharan, S. An insight on the electrocatalytic mechanistic study of pristine Ni MOF (BTC) in alkaline medium for enhanced OER and UOR. *ChemElectroChem* **2018**, *5*, 2795-2807.

(16) Wang, M.; Lin, M.; Li, J.; Huang, L.; Zhuang, Z.; Lin, C.; Zhou, L.; Mai, L. Metal–organic framework derived carbon-confined Ni₂P nanocrystals supported on graphene for an efficient oxygen evolution reaction. *Chem. Commun.* **2017**, *53*, 8372-8375.

(17) Zheng, X.; Zhang, B.; De Luna, P.; Liang, Y.; Comin, R.; Voznyy, O.; Han, L.; Garcia de Arquer, F. P.; Liu, M.; Dinh, C. T.; Regier, T.; Dynes, J. J.; He, S.; Xin, H. L.; Peng, H.; Prendergast, D.; Du, X.; Sargent, E. H. Theory-driven design of high-valence metal sites for water oxidation confirmed using in situ soft X-ray absorption. *Nat. Chem.* **2018**, *10*, 149-154.

(18) Rui, K.; Zhao, G.; Chen, Y.; Lin, Y.; Zhou, Q.; Chen, J.; Zhu, J.; Sun, W.; Huang, W.; Dou, S. X. Hybrid 2D dual-metal-organic frameworks for enhanced water oxidation catalysis. *Adv. Funct. Mater.* **2018**, *28*, 1801554.

(19) Zhao, S.; Wang, Y.; Dong, J.; He, C.-T.; Yin, H.; An, P.; Zhao, K.; Zhang, X.; Gao, C.; Zhang, L.; Lv, J.; Wang, J.; Zhang, J.; Khattak, A. M.; Khan, N. A.; Wei, Z.; Zhang, J.; Liu, S.; Zhao, H.; Tang, Z. Ultrathin metal–organic framework nanosheets for electrocatalytic oxygen evolution. *Nat. Energy* **2016**, *1*, 16184.